Suppression of Ionospheric Irregularity Due to Auroral Particle Impact

Toru Takahashi[1,2] , Andres Spicher[1,3] , Francesca Di Mare[1] , Douglas E. Rowland[4], Robert F. Pfaff[4], Michael R. Collier[4] , Lasse Boy Novock Clausen[1] , and Jøran Idar Moen[1,5]

[1]Department of Physics, University of Oslo, Oslo, Norway, [2]Electronic Navigation Research Institute, National Institute of Maritime, Port and Aviation Technology, Tokyo, Japan, [3]Department of Physics and Technology, The Arctic University of Norway, Tromsø, Norway, [4]NASA Goddard Space Flight Center, Greenbelt, MA, USA, [5]University Centre in Svalbard, Longyearbyen, Norway

Abstract The VISIONS-2 35.039 sounding rocket was launched from Ny-Ålesund, Svalbard, on 7 December 2018 at 11:06 UT, and traveled overhead of the cusp aurora. The payload reached an apogee of 806.6 km and provided measurements of the electric field (E) and electron density (N_e) with a high sampling rate of 6,250 Hz. The high-sampling-data make it possible to estimate the horizontal structure of E and N_e on scales ranging from meters to kilometers scale. The horizontal variation in the electron density and electric field ($\Delta N_e/N_e$ and ΔE) and integrated power of N_e and E (ΣP_{Ne} and ΣP_E) for 1–10, 10–100, and 100–1,000 Hz range were derived. The derived values were compared with the 557.7 and 630.0 nm emission intensities obtained from an all-sky camera installed in Ny-Ålesund projected at the footprint of the rocket, which was calculated by tracing the Earth's magnetic field line from the rocket altitude to the emission layer. $\Delta N_e/N_e$, ΔE, ΣP_{Ne}, and ΣP_E increased with the 630.0 nm emission intensity. Of particular interest is the lower level irregularity was observed when the 557.7 nm emission intensity exceeded 4.5 kR compared with other time interval. This may suggest that particle impact ionization created sufficient Pedersen conductance in the *E*-region to short the *F*-region current. This short-circuit seemed to cause the suppression of the irregularities in the *F*-region and lower level irregularities were also observed in the rocket altitude.

1. Introduction

The ionosphere plays an important role as a communication path between the ground and satellites. The irregularity of the plasma density is often generated from a few tens of kilometers to a few meters in the ionosphere (Weber et al., 1984). Notably, irregularities on the scale of hundreds of meters to a few kilometers cause fluctuations in the radio waves transmitted by the Global Navigation Satellite System satellites (Jin et al., 2016; Kintner et al., 2007).

Possible mechanisms for generating the ionospheric irregularities have been systematically investigated over the last four decades. Several generation mechanisms have been proposed, including gradient drift instability (GDI) (Lamarche & Makarevich, 2017; Moen et al., 2002; Ossakow et al., 1978; Reid, 1968; Spicher et al., 2015), Kelvin-Helmholtz instability (KHI) (Keskinen et al., 1988; Spicher et al., 2020), temperature gradient instability (Hudson & Kelley, 1987), and current-convective instability (Ossakow & Chaturvedi, 1979). In addition, Carlson (2012) suggested a two-step process of instability in which the KHI facilitates fast growth of GDI. Generation mechanisms originating from the auroral precipitation have also been proposed. LaBelle and Kintner (1989) and Kelley et al. (1982) resented the evidence that structured soft particle precipitation is an important source of large-scale irregularities (∼10s of km). Moen et al. (2012) observed decameter-scale irregularities spawned down from the km scale gradients, which were associated with auroral particle precipitation.

It is important to note that together with the irregularities, there is a polarization electric field that is caused by charge separation. The polarization electric field is immediately mapped along the magnetic field lines (Mozer, 1970) because of the high field-aligned conductance, and thus the irregularities are observable at a wide range of altitudes along the magnetic field lines. Kelley et al. (1982) proposed that the charge separation in the *F*-region could be partly canceled when the *E*-region conductance was high, and that then the plasma irregularities would be damped because of the short-circuit between the *E*- and *F*- regions. In the absence of sunrays, auroral particle impact ionization is the main driver of increased *E*-region conductivity at high latitudes. Therefore, simultaneous

observation of the irregularities and auroral precipitation is critically important to evaluating the effect of the *E*- and *F*-region coupling to the irregularity formation.

The auroral precipitation can be observed remotely by the all-sky camera, because it corresponds to the auroral emission intensity. On the other hand, we need to select which instrument to observe the irregularities according to their scale size. Since the irregularities appear with scales ranging from meters to kilometers scale, it is preferable to observe them on scales ranging from meters to kilometers. Although the radar remote sensing techniques, such as the European Incoherent Scatter radar and Super Dual Auroral Radar Network, have been frequently utilized to observe the irregularities, their spatiotemporal resolution is limited to investigate in detail the scales of interest here. Sounding rocket *in-situ* measurements can provide electron density and electric field data with a spatial resolution of several meters and temporal resolution of millisecond. By using the rocket data, several researchers have comprehensively presented irregularities with scales ranging from 10 to 1,000 m (Jin et al., 2019; Moen et al., 2012). Thus, sounding rocket observation is suitable for investigating the irregularity formation of small-to large-scale irregularities.

The combination of *in-situ* and ground-based observations makes it possible to investigate the irregularities associated with auroral particle precipitation. Irregularities caused by the particle precipitation will propagate upward because of the high mobility of electrons along the magnetic field lines. Therefore, the rocket can observe them. Furthermore, we can assess whether the irregularities are suppressed due to the increased conductance in the *E*-region, as suggested by Kelley et al. (1982). The purpose of this paper is to investigate the potential relationship between cusp particle precipitation and the formation of *F*-region plasma irregularities by using rocket *in-situ* and ground-based measurements.

2. VISIONS-2 Observation

The Visualizing Ion Outflow via Neutral Atom Sensing-2 (VISIONS-2) rockets were launched on 7 December 2018 from Ny-Ålesund (78.92°N, 11.93°E), Svalbard, as part of the Grand Challenge Initiative-Cusp (GCI-Cusp) project (Moen et al., 2018). VISIONS-2 consisted of two rockets (NASA 35.039 and NASA 35.040), which were launched at 11:06:00 and 11:08:00 UT, respectively. The rockets 35.039 and 35.040 reached apogees of 806,6 and 601,2 km in the flights lasting for about 950 and 800 s, respectively. In this work, we focus on results from the higher-apogee rocket, 35.039, utilizing data gathered with three different instruments:

1. A "multi-needle" Langmuir probe system (m-NLP) (Bekkeng et al., 2010; Jacobsen et al., 2010) provides the plasma density (N_e) and its variations at high cadence (6,250 samples/s) (Spicher et al., 2021).
2. Electric field (*E*) variations from a short, 1.1 m double probe that provided one component of the electric field vector at a sampling rate of 6,250 samples/s. As the payload was not spinning, this component was directed primarily in the zonal direction (east-west) for most of the flight.
3. Energetic electrons gathered at one pitch angle, primarily along the magnetic field direction (downward), in the range of 5.7–843.6 eV, with a full spectrum sampled approximately every 3 s by a MILENA-D spectrometer.

The high sampling rate of the density and electric field variations enabled estimation of the structure of N_e and *E* on scales of 10–1,000 m, as measured along the rocket trajectory. The rocket position (longitude, latitude, and altitude) was recorded at 20 Hz with an onboard Global Positioning System receiver.

The all-sky camera at Ny-Ålesund simultaneously captured 557.7 and 630.0 nm emissions at a cadence of 15 and 30 s intervals, with exposure times of 2,000 and 4,000 ms, respectively. During the rocket flight, there were thin clouds in the field of view (FOV) of the all-sky camera, so the emission intensity was subject to uncertainties. The FOV of the all-sky camera is shown in Figure 1. The emission layers are assumed to be 150 and 250 km for the 557.7 and 630.0 nm, respectively (Moen et al., 2001). The time series of cusp auroral formation is shown in Movie S1. The rocket trajectory, which is the time series of the aforementioned footprint in the 557.7 and 630.0 nm emission layers, is shown by the magenta lines in Figure 1 and the cross in Movie S1. The timestamp is the time of flight (TOF) in seconds, counting from 11:06:00 UT. Around 800 s before the launch, the cusp aurora span into the rocket trajectory. At 11:06 UT (0 s), the 35.039 rocked was launched in the south-west direction. The footprint of the rocket trajectory in the 557.7 and 630.0 nm emission layers encountered the poleward edge of the cusp aurora at around 370 s. After that, the cusp aurora expanded equatorward faster than the rocket. At around 630 s, the rocket footprint exited the cusp auroral region.
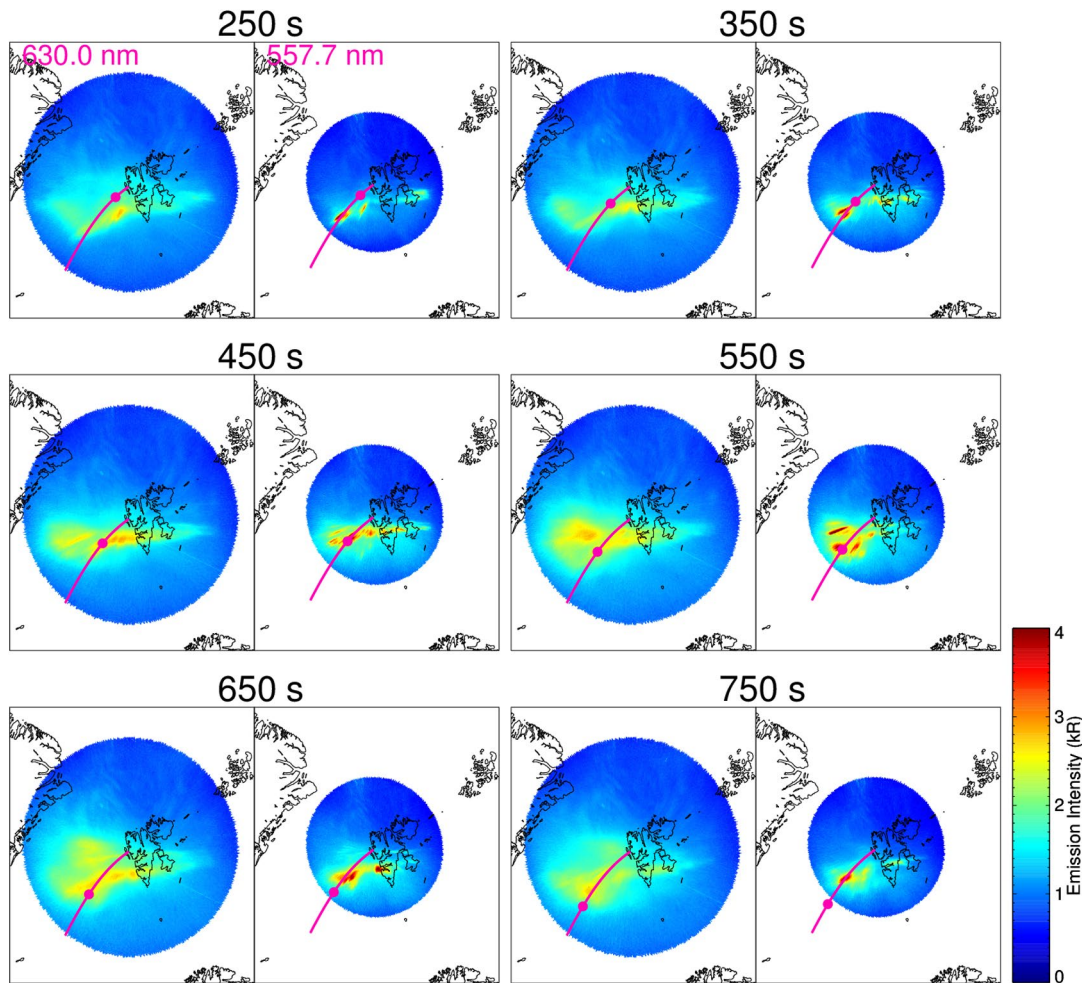
Figure 1. 557.7 and 630.0 nm all-sky images from 250 to 750 s with a 100 s time step. The magenta lines and dots indicate the trajectory of the rocket footprint and the rocket position.

It is essential to study the relationship between auroral emission intensity measured from the ground and the irregularities in N_e and E measured onboard the rocket. To compare the rocket data with the auroral emission intensity, the rocket position along the flight path was traced along the magnetic field line to the auroral emission layer at each data point, and the corresponding pixel in the all-sky camera was identified. The International Geomagnetic Reference Field model (Thébault et al., 2015) was used for the tracing shown in Figure 1. In this paper, the intersection of the traced magnetic field line and the emission layer is called the rocket footprint in the auroral emission layer.

Figure 2 shows an overview of the 35.039 rocket flight data. The horizontal axis indicates the TOF. The rocket altitude is shown in Figure 2a. N_e and E are shown in Figures 2b and 2c. The thick blue line in Figure 2b is the model electron density given by the International Reference Ionosphere (IRI) 2012 model (Bilitza et al., 2014). The electron density as obtained from the IRI model overestimated by a factor of 10 the observed data. Here, to identify the altitude range of auroral ionization by comparison of the observed and model altitude profile of N_e, the N_e given by the IRI was reduced to 10%. There is a large gap between the model and observed N_e below 350 km, the altitude reached at the beginning and at the end of the flight as indicated in the figure by the two vertical dashed lines. While there is some uncertainty in the m-NLP techniques used to derive the absolute electron density (Hoang et al., 2018), this behavior could suggest that the auroral particle ionization could have mainly occurred below that altitude. Polar cap patches can be seen as an increase in N_e density to twice that of the background density (Crowley et al., 1996; Spicher et al., 2017). In Figure 2b, there was no indication of large-scale polar cap patches, so that the particle precipitation appear to be the main driver of irregularities.
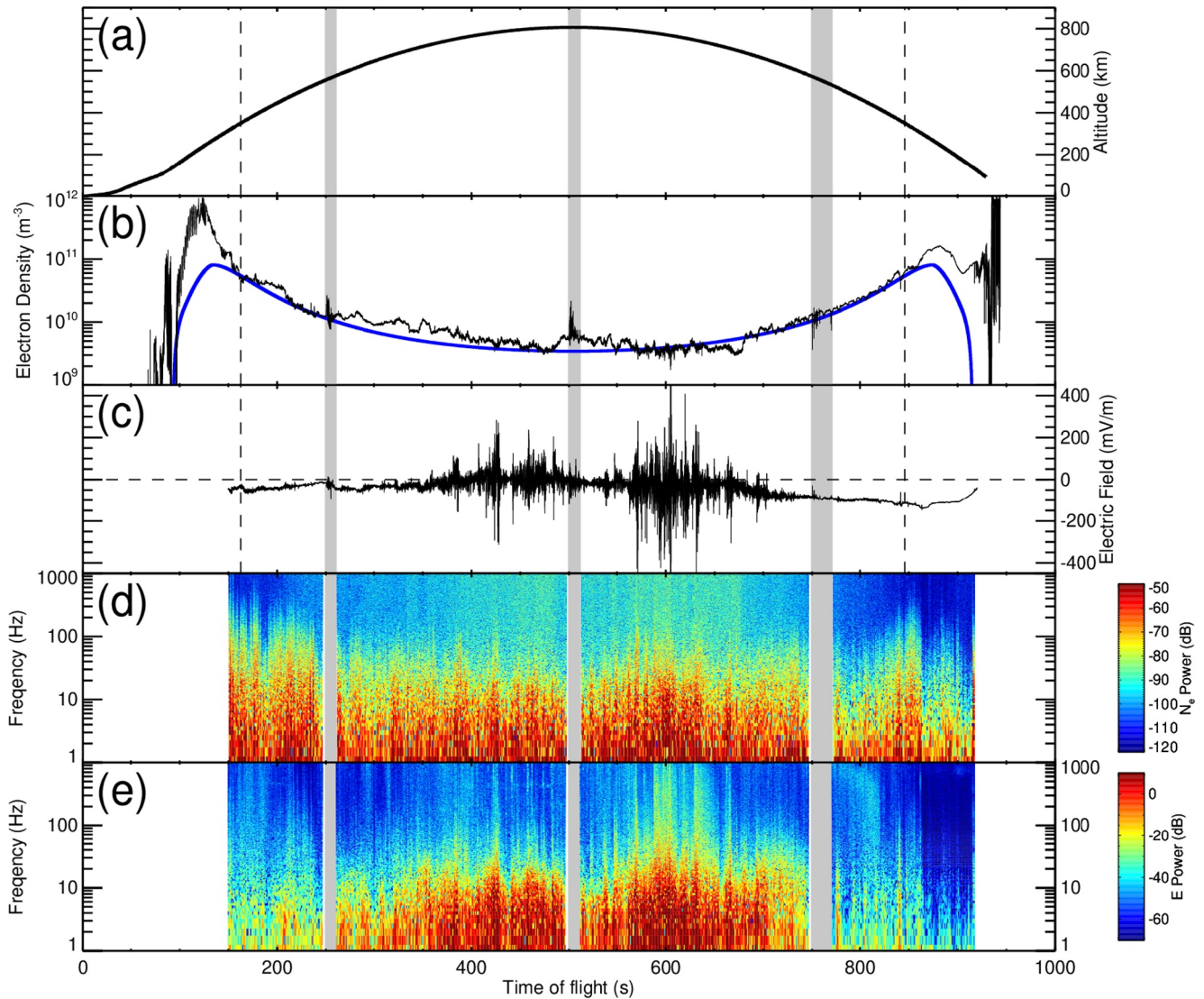
Figure 2. (a) The rocket altitude, (b) electron density (N_e) measured by the rocket (black line) and calculated with the International Reference Ionosphere model (blue line), (c) electric field E, the spectrograms for (d) N_e/N_{e0}, and (e) E. The parts shaded gray are the time intervals when the payload was maneuvering. The vertical dashed lines are the times when the rocket reached the altitude of 350 km.

Figure 2c shows the time series of E observed by the double probe with cross E field booms. The payload was roughly aligned with the magnetic field and the probes were located on booms deployed perpendicular to the main body. Before 375 s, the range of fluctuations was within about 50 mV/m, but after that, the fluctuations reached about $\pm\sim$200 mV/m in the time intervals 375–500 s and 550–700 s. The noise observed in the time intervals shaded gray is found in Figure 2b between 249–261, 499–512, and 749–771 s. These were due to maneuvering of the payload. Data obtained during those time intervals were omitted. Figures 2d and 2e show the spectrograms of N_e/N_{e0} and E. The spectrograms were calculated using a 2 s window and 1 s time step, where N_{e0} is the 2 s mean value of N_e.

In Figure 2d, the spectrogram of N_e/N_{e0} less than 10 Hz increased over course of the rocket flight. Before 200 s, the spectrogram of N_e/N_{e0} greater than 100 Hz was almost less than -100 dB, as shown by the blue color. From 300 to 750 s, it increased slightly above -90 dB and, color changes from blue to green/yellow. In Figure 2d, the spectrogram of N_e/N_{e0} less than display enhanced power spectral density ranging from 1 Hz to several hundreds of Hz over course of the rocket flight. Before 200 s, the spectrogram of N_e/N_{e0} greater than 100 Hz was almost less than -100 dB, as shown by the blue color. From 300 to 750 s, it increased slightly above -90 dB and, color

changes from blue to green/yellow. After 800 s, the color becomes blue again. This indicates the presence of small-scale structures from 300 to 750 s. In Figure 2e, the spectrogram of E enhanced below 10 Hz increased from 300 to 700 s, and at frequencies reaching to 1,000 Hz, it increased at about 600 s.

For this paper, we calculated the integrated power spectra (ΣP_{Ne} and ΣP_E) and horizontal variation ($\Delta N_e/N_e$ and ΔE) for N_e and E to evaluate the strength of the irregularities. Since the average rocket speed was about 800 m/s during the flight over the cusp aurora, the integration range was set to 1–10, 10–100, and 100–1,000 Hz correspond approximately to 1000, 100 and 10 s of m variations. The spectrogram was integrated using the log scale for the frequency. ΔN_e and ΔE are based on the rocket flight distance and indicate the variations in N_e and E over an arbitrarily chosen spatial scale. The calculation of ΔN_e and ΔE has already been described by Moen et al. (2012), but we also report briefly how it done here. The rocket flight distance x, ΔN_e and ΔE were calculated as follows:

$$t_1 = \frac{x}{v_r(t)} \tag{1}$$

$$\Delta N_e = |N_e(t) - N_e(t_1)| \tag{2}$$

$$\Delta E = |E(t) - E(t_1)| \tag{3}$$

where t_1 is the time taken by the rocket to travel distance x, and $v_r(t)$ is the rocket speed at t. In this paper, we derived the variations occurring over distance of 1000, 100 and 10 s of m by substituting those scale sizes to x. Finally, the N_e at t ($N_e(t)$ in Equation 2) was used to normalize the calculation of ΔN_e. We use ΔE (and not normalized), as done in previous studies (Basu et al., 1988). We investigated the relative differences in the data as shown in Equations 2 and 3, and considered large gradients to correspond to large irregularities, as done in Moen et al. (2012).

The scale size was based on the rocket speed. If the plasma structure changed and/or accelerated, the irregularity level at a particular scale-size could be over- or underestimated, and the irregularities would appear to decrease and/or increase because of Doppler effects. The change contributes to uncertainties in the categories 10, 100, and 1,000 m of the apparent scale-sizes calculated from Equations 2 and 3.

$\Delta N_e/N_e$ and ΔE are shown in Figure 3a (10 m), b (100 m), and c (1,000 m) with respect to TOF and altitude. As shown in Figures 2b and 2c, the time series of E and N_e fluctuated from 300 to 700 s. During this time interval, the 100 and 1,000 m scales of ΔE (the red lines in Figures 3b and 3c) reached to a normalized amplitude of 1.0 and 10 m scale of that (the red line in Figure 3a) reached 0.4. All scales of $\Delta N_e/N_e$ also increased above 0.2 in the same time interval. Around 600 s, both $\Delta N_e/N_e$ and ΔE increased simultaneously.

Figures 3d and 3e display ΣP_{Ne} and ΣP_E in 1–10, 10–100, and 100–1,000 Hz integration ranges. From 250 to 420 s, the ΣP_E in the 1–10 Hz range increased and reached its maximum value. It increased again around 600 s. Similar features can be seen in the 10–100 Hz range. The same kind of clear increase was not observed for ΣP_{Ne}, but it did increase slightly from 500 to 600 s in the 1–10 and 10–100 Hz range.

The above calculation method requires an assumption of spatiotemporal uniformity. The calculation of $\Delta N_e/N_e$ and ΔE used data points obtained within ~1.3 s and the spectrogram used a 2 s window. Since the rocket 35.039 traveled at an angle of less than 72 to the horizontal plane when above 350 km, the vertical flight distance was a maximum of three times larger than the horizontal one. If the rocket traveled 1,600 m horizontally in 2 s, its altitude also changed by up to 4,800 m. Thus we assumed that there was no significant spatiotemporal change in that horizontal and vertical directions within 2 s. Moreover the scale height of the topside ionosphere is about one order larger than 4,800 m (Belehaki et al., 2005).

Figure 3f shows the integrated electron energy flux observed by the MILENA-D onboard 35.039. The MILE-NA-D observed the energy flux of precipitated particles in the range of 5.7–843.6 eV. The integration was calculated as *Count rate* × *de* where *de* is the energy resolution. The integrated flux for high energy (>200 eV) is shown as the black line in Figure 3f. To compare the integrated energy flux and ground-based optical data, we integrated the energy flux in the ranges of <100 eV and >200 eV, which correspond to ionization altitude ranges of >350 km and 150–300 km, respectively (Millward et al., 1999). The integrated energy flux for >200 eV increased at 385.55 s. After 548.35 s, that time series repeatedly increased and decreased widely until 659.39 s.
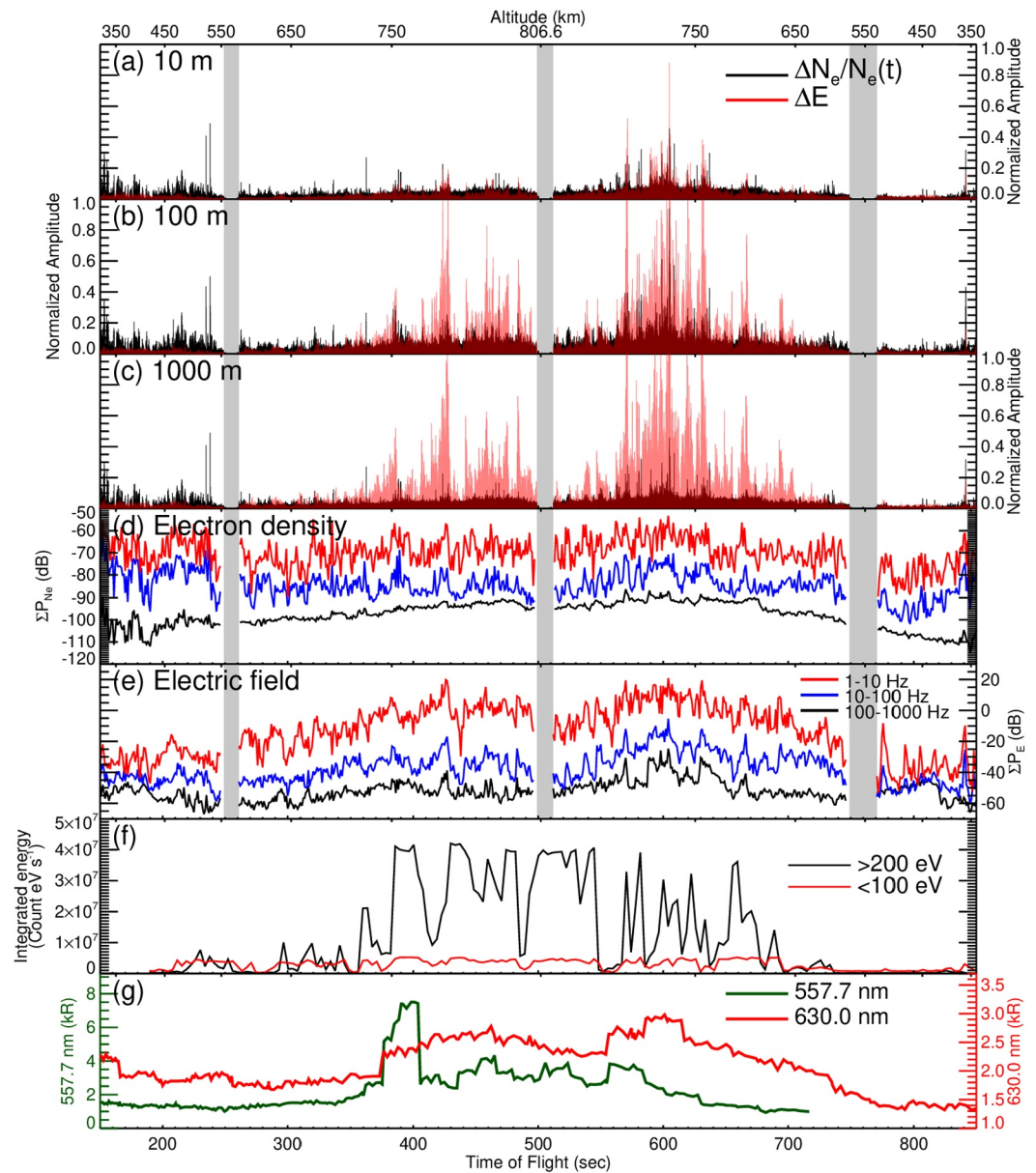
Figure 3. The variation in the density with respect to the average background density $\Delta N_e/N_e(t)$ (black line) and the variation in the electric field ΔE (red line) for the (a) 10 m, (b) 100 m and (c) 1,000 m scales. The integrated power as shown in Figures 2d and 2e in the 1–10, 10–100, and 100–1,000 Hz range for (d) the electron density and (e) electric field. (f) The integrated particle energy flux in the ranges <100 (red line) and >200 eV (black line). (g) The 557.7 (thick green line) and 630.0 nm emission intensities (thick red line) at the rocket footprint. The scales of the emission intensities are labeled on the left and right vertical axes for 557.7 and 630.0 nm. The top and bottom horizontal axes displays the rocket altitude and the TOF.

The MILENA-D was mounted in the center of the rocket deck. The MILENA-D electrostatic optics is a scaled version (1U) of that shown in Collier et al. (2015). The FOV is about 10 by 360 and was oriented perpendicular to the axis of the rocket. Although the integrated energy flux was calculated from the omni-directional data, we assumed the observed data was precipitated electrons. When the energy channel of MILENA-D changed, the Command and Data Handling started accumulating counts up to the saturation limit over the 100 ms dwell time. Certain energy channels sometimes saturated and it can be seen as a less dynamic response of integrated energy flux for >200 eV from 385.55 to 548.35 s. The electron data are purely descriptive in order to give an overview

of the experiment aboard the rocket, although they are not taken into account in the main analysis conducted in this study.

Figure 3g shows the time series of the 557.7 and 630.0 nm emission intensities. The emission intensity seemed to include the uncertainty because of the thin clouds in FOV of all sky camera and its uncertainty might be few kR. At 128 s, the rocket reached the 630.0 nm emission layer, which was assumed to peak at 250 km. At 368 s, the footprint in the 557.7 nm emission layer entered the bright auroral region, where the emission intensity was above 3.0 kR. At that time, the integrated energy flux for high energy increased. The 557.7 nm emission intensity at the rocket footprint increased drastically at 375 s from about 2.5 to 7.0 kR, but it rapidly decreased to about 3 kR at 405 s. After that, the 557.7 nm emission intensity sporadically showed increases up to about 4 kR in 450–465, 500–525, and 555–585 s. On the other hand, the 630.0 nm emission intensity varied moderately. The 630.0 nm emission intensity exceeded 2 kR after 375 s. After that, it remained in the range of 2.2–2.8 kR until 555 s. Around 600 s, it increased slightly, and reached a maximum value of 3.0 kR at 601 s. During this time interval, the integrated energy flux for high energy was not at the same level as in the previous time interval.

The direct comparison between the energy flux and the emission intensity appears rather complicated. We show here how the combined use of *in-situ* rocket data and all-sky camera observations allows us to characterize the presence of irregularities. From 375 to 405 s, the 557.7 nm emission intensity increased almost simultaneously with the integrated energy flux. After that, they tended to show almost similar trends. The time series of 630.0 nm emission did not show a clear correlation with the integrated energy flux, although the increasing trend around 400 s and decreasing after 600 s seems to be in agreement with the general trend of the integrated energy flux. The 557.7 nm emission intensity correlated with the integrated energy better than the 630.0 nm emission did. This could be because the time constant of excitation for the 557.7 nm emission is much smaller than that for the 630.0 nm emission. Furthermore, the different spatiotemporal resolutions between the energy flux of the *in-situ* rocket data and all-sky camera must be taken into account. Also the accuracy of footprint projection becomes lower as it separate from the center of the FOV for all-sky camera.

Comparison of the time series of the emission intensity at the footprint and the irregularities ($\Delta N_e/N_e$, ΔE, ΣP_{Ne}, and ΣP_E) showed the good agreement with each other. Hence, the rocket seemed to have observed irregularities associated with the auroral particle precipitation. In particular, the 630.0 nm emission seemed to correlate well with increased levels of $\Delta N_e/N_e$ and ΣP_E. However, increases in the 557.7 nm emission did not always correspond to increases in irregularities. From 375 to 405 s, when the 557.7 nm emission intensity reached 7.0 kR, both the electron density and electric field irregularities did not increase much compared with the irregularity increases observed around 600 s. This feature implies that the aurora dominated by the 557.7 nm emission was associated with the lower levels of irregularity. In the Section 3, we discuss this quantitatively.

3. Discussion

In Section 2, we calculated $\Delta N_e/N_e$, ΔE, ΣP_{Ne}, and ΣP_E, considered the irregularity component, and saw that they showed good agreement with the time series of the 630.0 nm emission, but that lower level irregularity was observed during the interval dominated by the 557.7 nm emission. In this section, we quantitatively compare the irregularity components and emission intensities. We discuss the altitude at which irregularities were generated in Section 3.1. Also, we suspected that the irregularities were suppressed during the time interval dominated by the 557.7 nm emission, and discuss the suppression scenario in Section 3.2.

3.1. Irregularities and Auroral Emission

The envelopes for $\Delta N_e/N_e$ and ΔE shown in Figures 3a–3c are calculated in order to correlate the time series of the electron density and electric field irregularity amplitudes. We defined the envelopes as the maximum values taken over intervals with lengths corresponding to the scale sizes selected. Figure 4 shows a comparison of $\Delta N_e/N_e$ (envelope), ΔE (envelope), ΣP_{Ne}, and ΣP_E and the emission intensities. Because the temporal resolution of the m-NLP and double probe were larger than that of the all-sky images, the medians of the envelopes for $\Delta N_e/N_e$ and ΣP_{Ne} were obtained while the footprint was located at the same pixel. Since the footprint moved in one pixel in times ranging from a few milliseconds to a few seconds, the medians were calculated over 1,000 data points. The medians of the envelopes for 10,100, and 1,000 m scales for ΔE (the red dots in Figures 4d–4f) varied widely
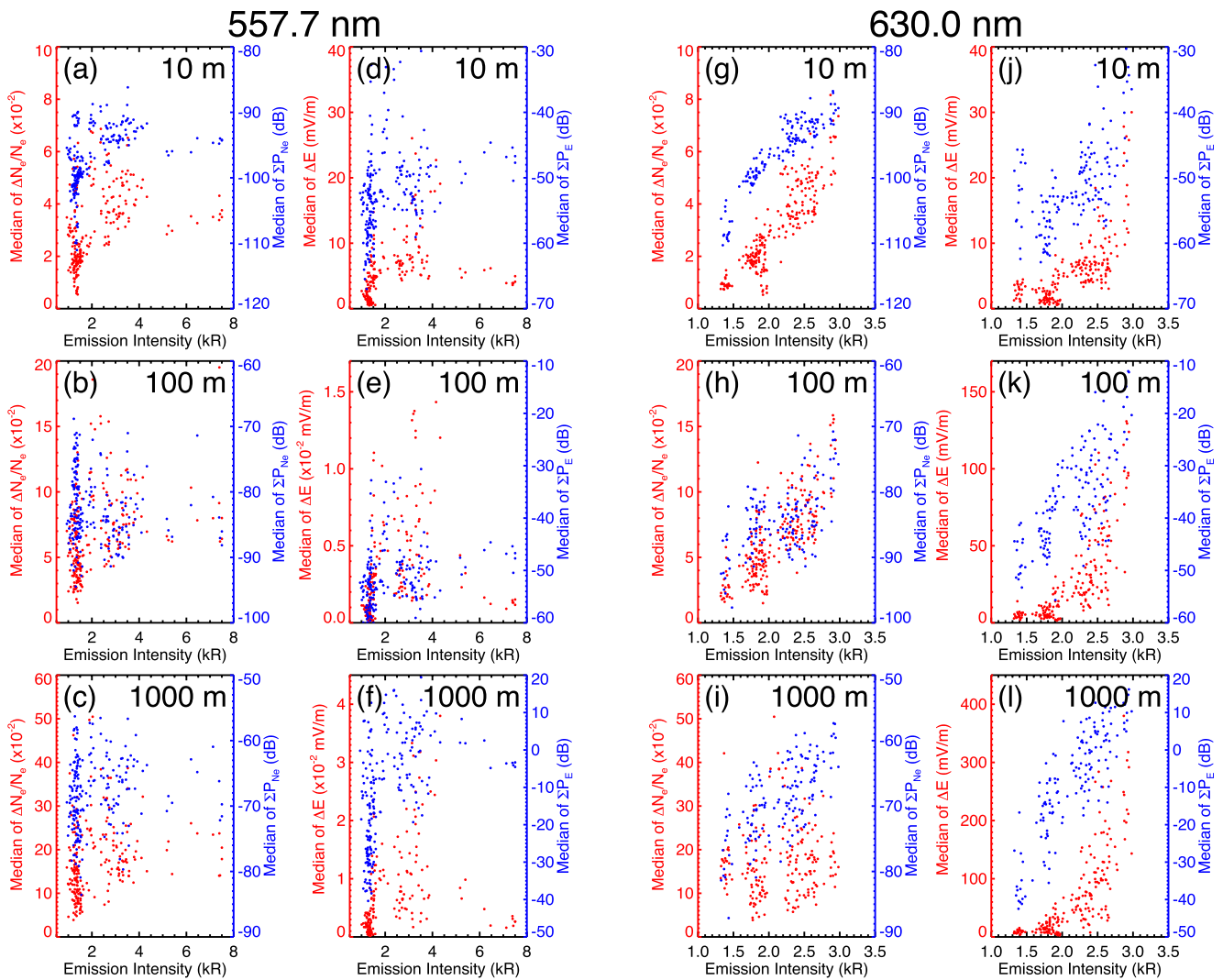
Figure 4. The medians of $\Delta N_e/N_e$ (envelope), ΔE (envelope), ΣP_{Ne}, and ΣP_E for the horizontal scales of 10, 100 and 1,000 m as related to the 557.7 nm (first and second columns from the left) and 630.0 nm (third and fourth columns) emission intensities. The red axes and dots show $\Delta N_e/N_e$ and ΔE, and the blue axes and dots show ΔE and ΣP_{Ne}. The panels in the top, middle and bottom rows are for the 10, 100, and 1,000 m scale irregularities.

when the 557.7 nm emission intensity was below 4.5 kR, but appeared to decrease when the 557.7 nm emission intensity was above 4.5 kR. In the other panels (Figures 4a–4c and the blue dots in Figures 4d–4f), there was no notable correlation when the 557.7 nm emission intensity was below 4.5 kR, and the medians of the envelopes for $\Delta N_e/N_e$, ΔE, ΣP_{Ne} and ΣP_E were roughly flat above 4.5 kR. Noteworthy is that none of the strong irregularities were observed in regions of the 557.7 nm emission above 4.5 kR. On the other hand, Figure 4g–l shows a good correlation between the medians of envelope for the irregularity values and 630.0 nm emission intensity. All panels display clear trends across the 630 nm data.

In addition to the correlation between the emission intensity and irregularities. Figure 4 also indicates that 10,100, and 1,000 m scale irregularities were observed simultaneously by the rocket. Although this feature suggests that the observed irregularities may have been caused by the spawn down from the larger-scale irregularities or by structured auroral precipitation, we cannot identify the cause of the irregularities unambiguously based on our datasets. It is also not possible to determine the generation altitude based on our observation data. However, Tsunoda (1988) mentioned that the meter-scale irregularities dissipates within seconds. Furthermore, Makarevich (2014) demonstrated a theoretical approach to the irregularity growth rate and indicated that the growth rate of the GDI process becomes small in the *E*-region because of collisions with neutral and charged particles. According to those studies, if the irregularities were generated in the *E*-region, 10 m scale irregularities would tend
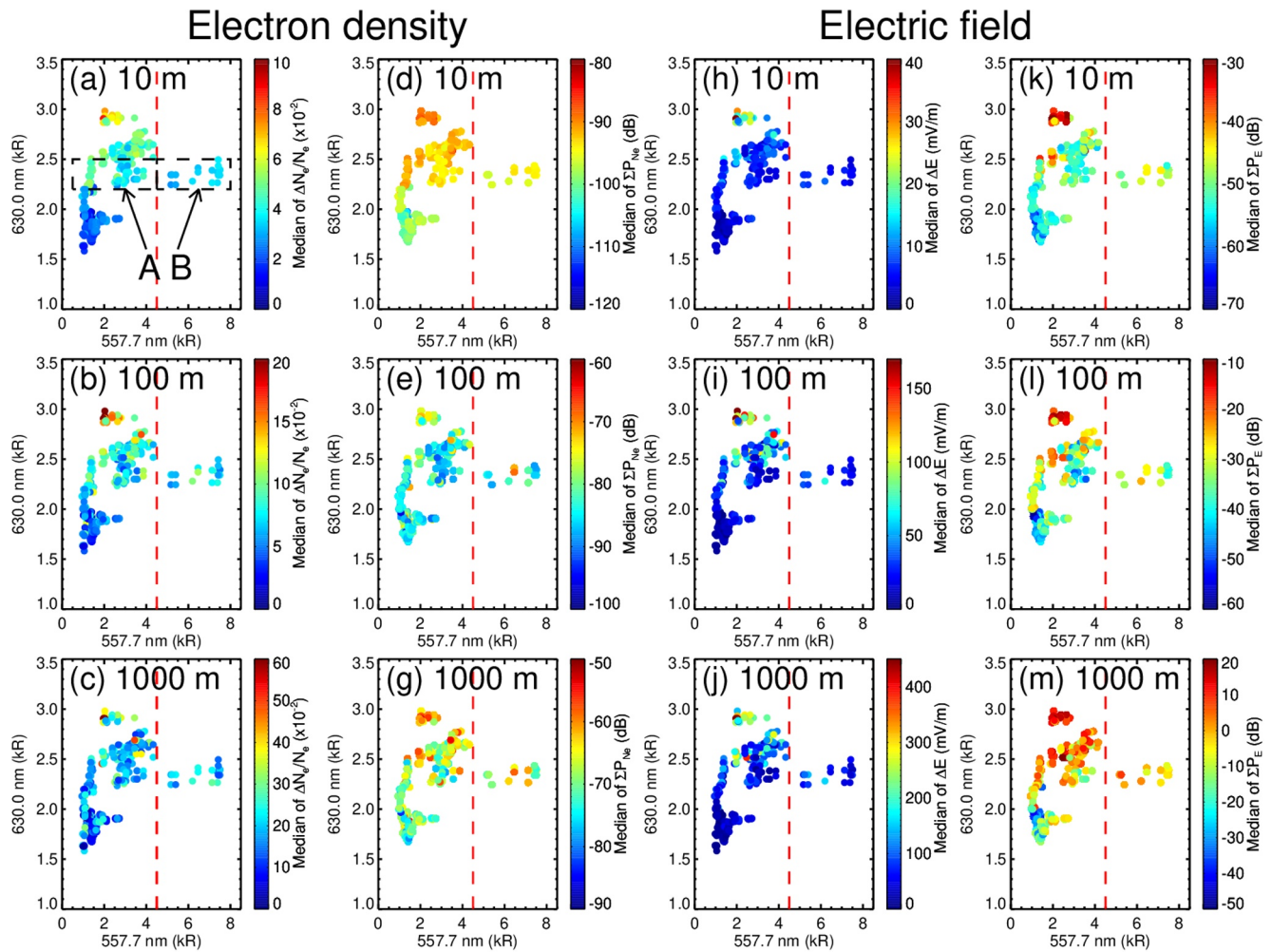
Figure 5. Comparison of emission intensity, $\Delta N_e/N_e$ (envelope), ΔE (envelope), ΣP_{Ne}, and ΣP_E for the 10, 100, and 1,000 m scales. The top, middle, and bottom panel rows are the 10, 100, and 1,000 m scales, respectively. The left, second, third, and right columns are $\Delta N_e/N_e$, ΔE, ΣP_{Ne}, and ΣP_E, respectively. The medians are indicated by the color scale. The box A and B indicates the range of 2.2–2.5 kR for the 630.0 nm and 0.5–4.5 kR and 4.5–8.0 kR for 557.7 nm.

to have a small growth rate, and decay rapidly. In our case, the 10 m scale irregularities were observed and showed similar correlation with the auroral emissions to that shown by large-scale irregularities (100 and 1,000 m). Thus, the observed irregularities may have been generated in the *F*-region.

3.2. Suppression of Irregularities

Of particular interest is the fact that the remarkable irregularity enhancements were not observed when the 557.7 nm emission intensity increased over 4.5 kR, whereas it increased with the 630.0 nm auroral emission enhancement. This was likely to imply that irregularities in the *F*-region were suppressed due to the conductance increasing in the *E*-region as suggested by Kelley et al. (1982) although the advection effect cannot be excluded. From 375 to 405 s, the 557.7 nm emission intensity increased drastically, and varied from 5.2 to 7.2 kR. In other time intervals, the intensity varied from ~1.0 to 4.2 kR. In our study, we separated the 557.7 nm emission intensity at 4.5 kR. During the time interval of the 557.7 nm emission increase, the 630.0 nm emission intensity varied from 2.2 to 2.5 kR.

Figure 5 shows a comparison of emission intensities using $\Delta N_e/N_e$ (envelope), ΔE (envelope), ΣP_{Ne}, and ΣP_E. The medians shown in Figure 4 are shown as cold to warm colors in Figure 5. The red dots tend to be located in the top left side of all panels. Apparently, there are no clear increases when the 557.7 nm emission intensity is greater than 4.5 kR. The data points contained in box A and box Bin Figure 5 have been set in order to evaluate whether

Table 1
The Ratios of $\Delta N_e/N_e$ and ΔE in Box A to Those in Box B Shown in Figure 5a, and the Differences Between ΣP_{Ne} and ΣP_E in Box A and Box B

Scale	Ratio (A/B)		Difference (A − B)	
	$\Delta N_e/N_e$	ΔE	ΣP_{Ne}	ΣP_E
10 m	1.29	2.16	2.76 (1.37)	−2.14 (0.78)
100 m	1.08	2.22	−0.52 (0.94)	−1.63 (0.83)
1,000 m	0.87	2.22	−1.02 (0.89)	0.75 (1.09)

Note. The values in brackets are the result of converting the differences into ratios.

the lower level irregularities were observed when the 557.7 nm emission increased above 4.5 kR. The range of box A and B are 0.0–4.5 kR (box A) and 4.5–8.0 kR (box B) for the 557.7 nm emission intensity, and 2.2–2.5 kR for the 630.0 nm. The irregularity in box A was obtained under the conditions of lower 557.7 nm emission intensity than that in box B.

The median of $\Delta N_e/N_e$ (envelope), ΔE (envelope), ΣP_{Ne}, and ΣP_E observed in the range of box A and B were calculated to derive the ratio and difference between them. Table 1 shows the ratio of box A to box B and the difference. The integrated power was calculated using the log scale, so the comparison of box A and box B is shown by the difference. A ratio over 1.00 and a positive difference value indicated that the lower level irregularities was observed in box A. As shown in Table 1, all of the ratios for $\Delta N_e/N_e$ and ΔE are greater than 1.00 except for the 1,000 m scale of $\Delta N_e/N_e$. The ratio suggest there was the lower level irregularities when the 557.7 nm emission intensity increased above 4.5 kR.

The difference can be converted to the ratio by $10^{(\text{Difference}/20)}$ under the assumption that the irregularities within the integration range increased by the same amount. The converted values are given in the brackets in Table 1. According to this, most of the difference values indicate the increasing of irregularities in the box B compared with those in box Aexcept for ΣP_{Ne} at the scale of the 10 m and ΣP_E at 1,000 m scale.

Results of the ratio are different from those of the difference. The range of 630.0 nm emission intensity in box A and Bwas set based on its variation when the 557.7 nm emission increased over 4.5 kR. The increased 557.7 nm emission intensities separated from those observed in other time intervals. However, there are a lot of data points for 630.0 nm emission intensity around the border of the range (horizontal dashed line for box A in Figure 5a). Thus, the different range of the 630.0 nm emission intensity should be also verified because the uncertainty of the all-sky camera measurement. If the range of 2.1–2.6 kR for 630.0 nm emission intensity was set, the values of the difference for 100 m scale for ΣP_{Ne} and ΣP_E became positive suggesting the lower level irregularity. Furthermore, if the range was set to 2.0–2.7 kR, the difference for the 100 m scale for ΣP_E became positive as well. On the other hand, the result of the ratio did not change. This suggests that the ratio is more accurate than the difference. The $\Delta N_e/N_e$ and ΔE were calculated between ∼0.013 and ∼1.3 s windows, but ΣP_{Ne}, and ΣP_E were calculated with a 2 s window. Also, the ΣP_{Ne} and ΣP_E were integrated values indicating the worse scale resolution of the irregularities. This may justify why the ratio and difference results appeared quite different. Finally, we considered that the lower level irregularities was likely to observed when the 557.7 nm emission intensity increased above 4.5 kR.

A suppression of irregularity and the advection effect are considered the cause which the lower level irregularity was observed above bright (>4.5 kR) 557.7 nm auroral emission. An ambient plasma including the irregularities moves by the $E \times B$ drift in the upper ionosphere. The vector of electric field was not observed so that it is difficult to evaluate the advection effect by our single rocket observation. In this paper, we discuss and evaluate the suppression mechanism of irregularity to describe that the lower level irregularity was observed when the 557.7 nm emission increased.

The E- and F-regions couple at the Alfvén velocity (∼ 2000 km/s (Lysak, 1990)), and the time constant of the coupling is estimated to be 0.3 s. Since that time constant is much shorter than the temporal resolution of the all-sky camera, the coupling process may be considered to be one of the possible mechanisms for the suppression of irregularities. The 557.7 nm emission increase indicates a conductance increase in the E-region (Kosch et al., 2001; Mende et al., 1984; Oyama et al., 2013). When the E-region conductance increases, the E- and F-regions become electrically coupled. Thereby, the field-aligned currents ($J_\parallel$) are short-circuited by a Pedersen current (J_P) in the E-region. Takahashi et al. (2019) suggested that these electrons play a role of partly canceling the charge separation. Kelley et al. (1982) also suggested that this cancellation causes damping of the growth of irregularities in the F-region.

We propose the following scenario for the suppression of irregularities in Figure 6. When the 557.7 nm emission intensity was less than 4.5 kR, irregularities were generated in the F-region and mainly propagated upward along the magnetic field lines. When the 557.7 nm emission intensity increases to above 4.5 kR, the electrons became able to move freely between the E- and F-regions. When this happened, the charge separation in the F-region was
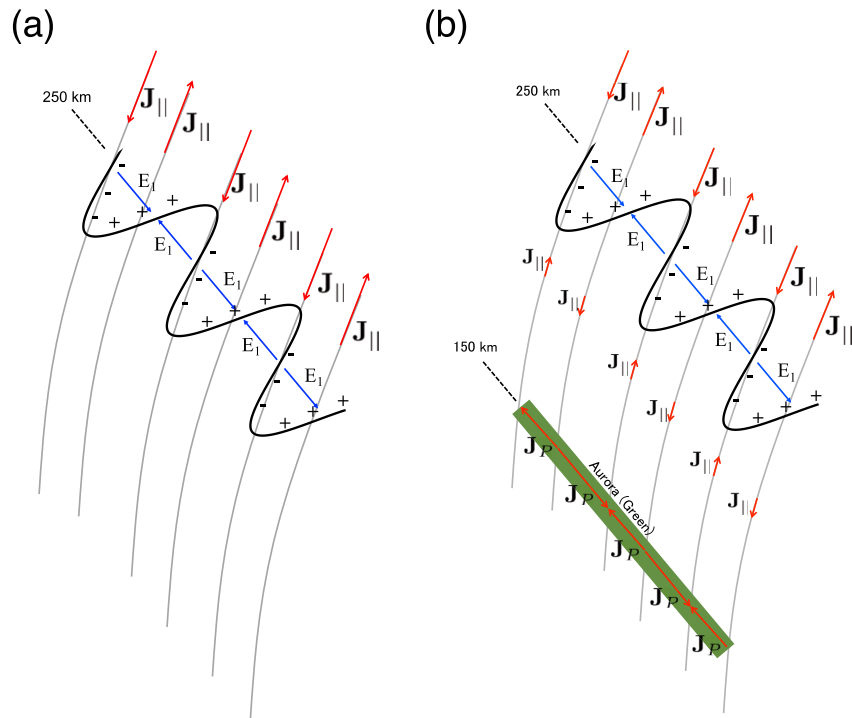
Figure 6. The scenario for the generation and propagation of irregularities along a magnetic field line (thick black curves), the field-aligned $J_{\parallel}$ (red arrows). (a) The polarization electric field propagating upward to the rocket altitude along the magnetic field line. (b) The suppression of irregularities accompanying the Pedersen current J_P and the green aurora emission.

partly canceled, and thus, the irregularities in the F-region was suppressed. Then, the lower level irregularities at the rocket altitude were observed.

The mechanism of suppression is illustrated in Figure 6. The 557.7 and 630.0 nm emission intensities ($I_{557.7}$ and $I_{630.0}$) correspond to the ionospheric conductance, which is proportional to the electron density (Kosch et al., 2001; Mende et al., 1984; Oyama et al., 2013). Oyama et al. (2013) provided the following function to express the relationship between the emission intensity and ionospheric conductance quantitatively:

$$\Sigma_P = 1.1 \times 10^{-1} \sqrt{I_{557.7}} - 2.1 \times 10^{-1} \qquad \text{S} \qquad (4)$$

where Σ_P is the height-integrated Pedersen conductance. The integration height is 110–170 km.

Since there were thin clouds above Longyearbyen, the emission intensity was subject to uncertainties. Although we cannot estimate the uncertainties using our data set, the measurement error for $I_{557.7}$ was roughly assumed to be 2.0 kR in our study. The error values of 1.1×10^{-1} and -2.1×10^{-1} can be ignored because they are considered to be much less than the uncertainties in $I_{557.7}$ (Oyama et al., 2013). According to this equation, 4.5 (± 2.0) kR corresponds to $\Sigma_P = 7.2$ (± 1.6) S in the E-region. We suggest that this conductance is likely to be a threshold for efficiently suppressing F-region plasma irregularities in this event.

4. Conclusions

The VISIONS-2 35.039 rocket was launched from Ny-Ålesund, Svalbard on 7 December 2018 at 11:06 UT. During the rocket flight, an all-sky camera with the 557.7 and 630.0 nm optical filters captured the images simultaneously. According to the all-sky camera observations, the rocket traveled overhead of the cusp aurora. An m-NLP and double probe onboard the rocket measured N_e and E with a high sampling rate of 6,250 Hz. The high-sampling-rate data enabled us to estimate the horizontal structure of the electron density and electric field on scales ranging from meters to kilometers.

The 557.7 and 630.0 nm emission intensities were compared with the 10, 100, and 1,000 m scale of $\Delta N_e/N_e$, ΔE, ΣP_{Ne}, and ΣP_E. The 10, 100, and 1,000 m scale irregularities clearly increased with increase in the 630.0 nm emission intensity. However, the lower level irregularity was observed when the 557.7 nm emission intensity exceeded 4.5 kR compared with other time interval. By comparing the 557.7 and 630.0 nm emission intensities, $\Delta N_e/N_e$, ΔE, ΣP_{Ne}, and ΣP_E, we discovered that the irregularities seemed to be suppressed during the increase in the the 557.7 nm emission, although the advection effect cannot be excluded. Based on these analysis results, we conclude that the following scenario might be able to explain the generation and suppression of irregularities in this event.

The 10,100, and 1,000 m scale irregularities were generated in the *F*-region by a mechanism associated with the auroral particle precipitation. When the 557.7 nm emission intensity increased, the *E*-region conductance increased. When that happened, the *E*- and *F*-regions became electrically coupled, and therefore a short-circuit was induced via the field-aligned ($J_\parallel$) and Pedersen current (J_P). This is turn cause the suppression of irregularities in the *F*-region. Furthermore, the threshold for the suppression of irregularities seemed to be $\Sigma_P = 7.2$ (± 1.6) S, equivalent to a value of 4.5 kR for the 557.7 nm emission intensity in the *E*-region.

Data Availability Statement

The all-sky camera data can be obtained from http://tid.uio.no/plasma/aurora/tech.html. The IRI data can be downloaded from https://ccmc.gsfc.nasa.gov/modelweb/models/iri2012_vitmo.php. The rocket data are being archived on the Space Physics Data Facility, https://spdf.gsfc.nasa.gov/. The m-NLP data can be obtained from https://doi.org/10.11582/2021,00004.

References

Basu, S., Basu, S., MacKenzie, E., Fougere, P. F., Coley, W. R., Maynard, N. C., et al. (1988). Simultaneous density and electric field fluctuation spectra associated with velocity shears in the auroral oval. *Journal of Geophysical Research*, *93*(A1), 115–136. https://doi.org/10.1029/JA093iA01p00115

Bekkeng, T. A., Jacobsen, K. S., Bekkeng, J. K., Pedersen, A., Lindem, T., Lebreton, J.-P., & Moen, J. I. (2010). Design of a multi-needle Langmuir probe system. *Measurement Science and Technology*, *21*(8), 085903. https://doi.org/10.1088/0957-0233/21/8/085903

Belehaki, A., Marinov, P., Kutiev, I., Jakowski, N., & Stankov, S. (2005). Comparison of the topside ionosphere scale height determined by topside sounders model and bottom side digisonde profiles. *Advances in Space Research*, *37*(5), 963–966. https://doi.org/10.1016/j.asr.2005.09.014

Bilitza, D., Altadill, D., Zhang, Y., Mertens, C., Truhlik, V., Richards, P., & Reinisch, B. (2014). The international reference ionosphere 2012—A model of international collaboration. *Journal of Space Weather and Space Climate*, *4*, 1–12. https://doi.org/10.1051/swsc/2014004

Carlson, H. C. (2012). Sharpening our thinking about polar cap ionospheric patch morphology, research, and mitigation techniques. *Radio Science*, *47*. https://doi.org/10.1029/2011RS004946

Collier, M. R., Chornay, D., Clemmons, J., Keller, J., Klenzing, J., Kujawski, J., & Zettergren, M. (2015). Visions remote observations of a spatially-structured filamentary source of energetic neutral atoms near the polar cap boundary during an auroral substorm. *Advances in Space Research*, *56*(10), 2097–2105. https://doi.org/10.1016/j.asr.2015.08.010

Crowley, G., Schoendorf, J., Roble, R. G., & Marcos, F. A. (1996). Cellular structures in the high-latitude thermosphere. *Journal of Geophysical Research*, *101*(A1), 211–223. https://doi.org/10.1029/95JA02584

Hoang, H., Røed, K., Bekkeng, T. A., Moen, J. I., Spicher, A., Clausen, L. B. N., & Pedersen, A. (2018). A study of data analysis techniques for the multi-needle langmuir probe. *Measurement Science and Technology*, *29*. https://doi.org/10.1088/1361-6501/aab948

Hudson, M. K., & Kelley, M. C. (1987). The temperature gradient drift instability at the equatorward edge of the ionospheric plasma trough. *Journal of Geophysical Research*, *81*. https://doi.org/10.1029/JA081i023p03913

Jacobsen, K. S., Pedersen, A., Moen, J. I., & Bekkeng, T. A. (2010). A new Langmuir probe concept for rapid sampling of space plasma electron density. *Measurement Science and Technology*, *21*. https://doi.org/10.1088/0957-0233/21/8/085902

Jin, Y., Moen, J. I., Miloch, W. J., Clausen, L. B. N., & Oksavik, K. (2016). Statistical study of the gnss phase scintillation associated with two types of auroral blobs. *Journal of Geophysical Research: Space Physics*, *121*. https://doi.org/10.1002/2016JA022613

Jin, Y., Moen, J. I., Spicher, A., Oksavik, K., Miloch, W. J., Clausen, L. B. N., & Saito, Y. (2019). Simultaneous rocket and scintillation observations of plasma irregularities associated with a reversed flow event in the cusp ionosphere. *Journal of Geophysical Research: Space Physics*, *124*, 7098–7111. https://doi.org/10.1029/2019JA026942

Kelley, M. C., Vickrey, J. F., Carlson, C. W., & Torbert, R. (1982). On the origin and spatial extent of high-latitude f region irregularities. *Journal of Geophysical Research*, *87*(A6), 4469–4475. https://doi.org/10.1029/JA087iA06p04469

Keskinen, M. J., Mitchel, H. G., Fedder, J. A., Satyanarayana, P., Zalesak, S. T., & Huba, J. D. (1988). Nonlinear evolution of the kelvin-helmholtz instability in the high-latitude ionosphere. *Journal of Geophysical Research*, *93*, 137–152. https://doi.org/10.1029/JA093iA01p00137

Kintner, P. M., Ledvina, B. M., & de Paula, E. R. (2007). Gps and ionospheric scintillations. *Space Weather*, *5*, S09003. https://doi.org/10.1029/2006SW000260

Kosch, M. J., Honary, F., del Pozo, C. F., Marple, S. R., & Hagfors, T. (2001). High-resolution maps of the characteristic energy of precipitating auroral particles. *Journal of Geophysical Research*, *106*(A12). https://doi.org/10.1029/2001JA900107

LaBelle, J., & Kintner, P. M. (1989). The measurement of wavelength in space plasmas. *Review of Geophysics*, *27*(4), 495–518. https://doi.org/10.1029/RG027i004p00495

Lamarche, L. J., & Makarevich, R. A. (2017). Radar observations of density gradients, electric fields, and plasma irregularities near polar cap patches in the context of the gradient-drift instability. *Journal of Geophysical Research: Space Physics*, *122*, 3721–3736. https://doi.org/10.1002/2016JA023702

Lysak, R. L. (1990). Propagation of alfven waves through the ionosphere: Dependence on ionospheric parameters. *Journal of Geophysical Research*, *104*(A5), 017–030. https://doi.org/10.1029/1999JA900024

Makarevich, R. A. (2014). Symmetry considerations in the two-fluid theory of the gradient drift instability in the lower ionosphere. *Journal of Geophysical Research: Space Physics*, *119*, 7902–7913. https://doi.org/10.1002/2014JA020292

Mende, S. B., Eather, R. H., Rees, M. H., Vondrak, R. R., & Robinson, R. M. (1984). Optical mapping of ionospheric conductance. *Journal of Geophysical Research*, *89*, 1755–1763. https://doi.org/10.1029/JA089iA03p01755

Millward, G. H., Moffett, R. J., Balmforth, H. F., & Rodger, A. S. (1999). Modeling the ionospheric effects of ion and electron precipitation in the cusp. *Journal of Geophysical Research*, *104*, 24603–24612. https://doi.org/10.1029/1999JA900249

Moen, J., Carlson, H. C., Milan, S. E., Shumilov1, N., Lybekk, B., Sandholt, P. E., & Lester, M. (2001). On the collocation between dayside auroral activity and coherent hf radar backscatter. *Annales Geophysicae*, *18*, 1531–1549. https://doi.org/10.1007/s00585-001-1531-2

Moen, J., Oksavik, K., Abe, T., Lester, M., Saito, Y., Bekkeng, T. A., & Jacobsen, K. S. (2012). First in-situ measurements of hf radar echoing targets. *Geophysical Research Letters*, *39*. https://doi.org/10.1029/2012GL051407

Moen, J., Spicher, A., Rowland, D., Kletzing, C., & LaBelle, J. (2018). Grand challenge initiative-cusp: Rockets to explore solar wind-driven dynamics of the top side polar atmosphere. In SESS 2018 the state of environmental science in svalbard. *Longyearbyen: Svalbard Integrated Arctic Earth Observing System*, (pp. 184–204).

Moen, J., Walker, I. K., Kersley, L., & Milan, S. E. (2002). On the generation of cusp hf backscatter irregularities. *Journal of Geophysical Research*, *107*(A4). https://doi.org/10.1029/2001JA000111

Mozer, F. S. (1970). Electric field mapping in the ionosphere at the equatorial plane. *Planetary and Space Science*, *18*, 259–263. https://doi.org/10.1016/0032-0633(70)90161-3

Ossakow, S. L., & Chaturvedi, P. K. (1979). Current convective instability in the diffuse aurora. *Journal of Geophysical Research*, *6*. https://doi.org/10.1029/GL006i004p00332

Ossakow, S. L., Chaturvedi, P. K., & Workman, J. B. (1978). High-altitude limit of the gradient drift instability. *Journal of Geophysical Research*, *83*. https://doi.org/10.1029/JA083iA06p02691

Oyama, S., Watanabe, T., Fujii, R., Nozawa, S., & Tsuda, T. T. (2013). Estimation of the layered ionospheric conductance using data from a multi-wavelength photometer at the european incoherent scatter (eiscat) radar site. *Antarctic Record*, *57*(3), 339–356.

Reid, G. C. (1968). The formation of small-scale irregularities in the ionosphere. *Journal of Geophysical Research*, *73*(5), 1627–1640. https://doi.org/10.1029/JA073i005p01627

Spicher, A., Bang-Hauge, & Trondsen, D. M. E. (2021). Om-nlp on visions-2 35.039. [data set]. https://doi.org/10.11582/2021.00004

Spicher, A., Cameron, T., Grono, E. M., Yakymenko, K. N., Buchert, S. C., Clausen, L. B. N., & Moen, J. I. (2015). Observation of polar cap patches and calculation of gradient drift instability growth times: A swarm case study. *Geophysical Research Letters*, *42*, 201–206. https://doi.org/10.1002/2014GL062590

Spicher, A., Clausen, L. B. N., Miloch, W. J., Lofstad, V., Jin, Y., & Moen, J. I. (2017). Nterhemispheric study of polar cap patch occurrence based on swarm in situ data. *Journal of Geophysical Research: Space Physics*, *122*, 3837–3851. https://doi.org/10.1002/2016JA023750

Spicher, A., Deshpande, K., Jin, Y., Oksavik, K., Zettergren, M. D., & Baddeley, L. (2020). On the production of ionospheric irregularities via kelvin-helmholtz instability associated with cusp flow channels. *Journal of Geophysical Research: Space Physics*, *125*, e2019JA027734. https://doi.org/10.1029/2019JA027734

Takahashi, T., Virtanen, I. I., Hosokawa, K., Ogawa, Y., Aikio, A., Miyaoka, H., & Kero, A. (2019). Polarization electric field inside auroral patches: Simultaneous experiment of EISCAT radars and KAIRA. *Journal of Geophysical Research: Space Physics*, *124*, 3543–3557. https://doi.org/10.1029/2018JA026254

Thébault, E., Finlay, C. C., Beggan, C. D., Alken, P., Aubert, J., Barrois, O., & Zvereva, T. (2015). International geomagnetic reference field: The 12th generation. *Earth, Planets and Space*, *67*. https://doi.org/10.1186/s40623-015-0228-9.79

Tsunoda, R. T. (1988). High-latitude f region irregularities: A review and synthesis. *Reviews of Geophysics*, *26*(4), 719–760. https://doi.org/10.1029/RG026i004p00719

Weber, E. J., Buchau, J., Moore, J. G., Sharber, J. R., Livingston, R. C., Winningham, J. D., & Reinisch, B. W. (1984). F layer ionization patches in the polar cap. *Journal of Geophysical Research*, *89*, 1683–1694. https://doi.org/10.1029/JA089iA03p01683